Physics of Fluids

RESEARCH ARTICLE | FEBRUARY 09 2024

Path selection of liquid fronts in junctions of branching channels

Sohyun Jung ; Tae Jeong Kim ; Jae Hong Lee ; Wonjong Jung ; Ho-Young Kim

Check for updates

Physics of Fluids 36, 022107 (2024)
https://doi.org/10.1063/5.0185861

View Online
Export Citation

Articles You May Be Interested In

Capillary rise on rounded polygon corners of pillar and array structures

Physics of Fluids (October 2024)

Wicking pumps for microfluidics

Biomicrofluidics (November 2024)

A bionic microdroplet array chip for particle trapping

Physics of Fluids (January 2025)

20 March 2025 13:25:23

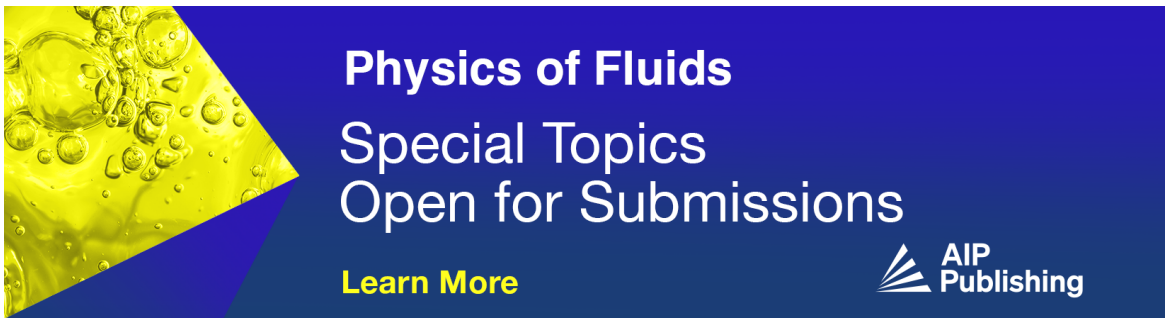

AIP Publishing

Physics of Fluids ARTICLE pubs.aip.org/aip/pof

Path selection of liquid fronts in junctions of branching channels

Cite as: Phys. Fluids **36**, 022107 (2024); doi: 10.1063/5.0185861
Submitted: 2 November 2023 · Accepted: 17 January 2024 ·
Published Online: 9 February 2024

View Online Export Citation CrossMark

Sohyun Jung,[1] Tae Jeong Kim,[1] Jae Hong Lee,[2] Wonjong Jung,[3,a)] and Ho-Young Kim[1,4,a)]

AFFILIATIONS

[1]Department of Mechanical Engineering, Seoul National University, Seoul 08826, Korea
[2]Samsung Advanced Institute of Technology, Suwon, Gyeonggi-do 16678, Korea
[3]Department of Mechanical, Smart, and Industrial Engineering, Gachon University, Seongnam, Gyeonggi-do 13120, Korea
[4]Institute of Advanced Machines and Design, Seoul National University, Seoul 08826, Korea

[a)]Authors to whom correspondence should be addressed: wonjongjung@gachon.ac.kr and hyk@snu.ac.kr

ABSTRACT

We consider how a liquid front propagating through an initially dry channel network selects its path when encountering branch junctions. We employ both experimental observation and theoretical analysis to investigate the path selection dynamics depending on liquid properties, pressure-driven flow rate, and channel geometry. We identify three distinct front propagation types at the junction, namely, straight, diverging, and diverting flows, and construct their regime map with theoretical regime boundaries. These flow types at the junction determine the subsequent channel-filling patterns, which we also identify and categorize. Our results allow us to design small-scale channel networks to precisely deliver or distribute functional liquids, which can be applied to lab-on-a-chip systems, liquid sculpture, and porous flow control.

Published under an exclusive license by AIP Publishing. https://doi.org/10.1063/5.0185861

20 March 2025 13:25:23

I. INTRODUCTION

When a liquid is injected into a channel network initially filled with another fluid, it displaces the pre-occupying fluid and propagates through the channel. The filling of fluid networks forms a fundamental basis of various industrial processes, including microfluidics,[1] desalination,[2,3] injection molding,[4,5] and oil and gas production.[6,7] These applications frequently involve complicated channel networks consisting of multiple branches, whether they are formed artificially or naturally (e.g., porous media like rocks and soil beds). While the propagation dynamics of liquid in a simple uniform channel is classical,[8–17] it is challenging to predict or control the propagation patterns in branching channels.

As the liquid flows through a branching channel, the specific path taken by its propagation front at the junction determines the subsequent flow pattern because the liquid tends to follow the preexisting path that provides the minimum resistance. If we understand how such path selection occurs at the junction, we can either tune the network geometry or vary the liquid condition in order to deliver the liquid to desired locations. Furthermore, steering the liquid fronts that lead streams allows us to architect the liquid, which can be used to emulate biological fluid network or for free-form fabrication.[18–21]

In milli- or microfluidic systems using wettable solids and slow viscous liquid flows,[22–25] the liquid infiltration can be driven by capillarity while resisted by viscosity. Then, the path selection of the inertialess flow is determined by minimization of the surface free energy, which allows for relatively simple prediction based on the channel geometry.[26] Without resorting to capillarity, liquids can be actively forced into channels for faster filling or overcoming excessive viscous resistance, as can be seen in microfluidic array for sample loading,[27–29] pressurized underfill encapsulation of flip chips,[30,31] and injection molding.[4,5] Gravity can also drive liquid flows through natural rocks with a network of cracks, which is of geological implications, such as groundwater recharge[32] and oil and gas migration.[33]

Our interest in this work lies in the path selection mechanism and the consequent liquid-filling patterns as a liquid is pumped into orthogonally branching networks. We combine experiment and theory to understand how the liquid properties, injection flow rate, and the channel geometry affect the liquid front's path selection at branch junctions. We build a regime map for the propagation front behavior, with a theoretical account of the regime boundaries. We also show that the different path selections allow us to obtain diverse liquid-filling patterns.

II. EXPERIMENTAL

Our model system, as shown in Fig. 1, consists of a main straight channel with the width w_m and depth h intersecting perpendicularly

Published under an exclusive license by AIP Publishing

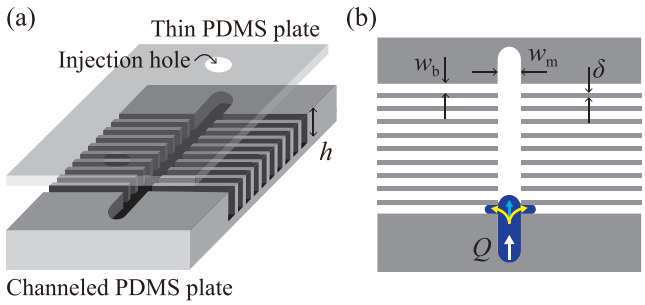

FIG. 1. (a) A bird-eye view schematic of a multi-branching channel formed on a PDMS plate that is topped with another thin transparent PDMS plate. (b) A top view schematic of the channel.

with branching channels of the width w_b. Adjacent branching channels maintain a consistent spacing of δ. In our experiments, w_m is either 1 or 3 mm and w_b ranges from 0.3 to 3 mm, while h and δ are, respectively, maintained constant at 3 mm and 500 μm, respectively.

We fabricated the channels by pouring PDMS (polydimethylsiloxane) onto a mold with three-dimensional printed channel patterns. The resulting channeled PDMS plate was then bonded to another PDMS plate, 4 mm in thickness, via oxygen plasma treatment. The inner walls of these channels were also treated with oxygen plasma to achieve hydrophilicity just before supplying a liquid into the chip through a hole in the top plate. The liquid flow was driven by a syringe pump at a pre-set constant flow rate ranging from 80 to 2800 $\mathrm{mm^3\,s^{-1}}$ into the horizontally situated branching channels. The liquids were aqueous ethanol solutions with the volume concentration of ethanol ranging from 0% to 25%. A water-soluble dye (Food Blue No. 1-A, Lites) was added to each solution at the concentration of 0.0005 wt. %.

We observed the liquid front's behavior, particularly its propagation and path selection at the junctions of branching channels, using a high-speed camera (SA1.1, Photron) operating at frame rates ranging from 250 to 1000 $\mathrm{s^{-1}}$. The liquid velocity at these junctions was measured by tracking the displacement of the liquid front, as detailed in Sec. III A.

In addition, we measured the density ρ, viscosity μ, and surface tension coefficient σ of the dyed liquids with different ethanol concentrations; these were carried out using a viscometer (SV-10, A&D) and a surface-tension-meter (K-100, KRUSS). We also measured the static as-placed contact angle of 2 μl volume droplets of each liquid on the oxygen plasma-treated PDMS surfaces. The critical advancing contact angle was measured by supplying liquid in a static drop through a syringe until the contact line begins to advance.[34] The results are listed in Table I.

III. RESULTS AND DISCUSSION

A. Liquid front behaviors at the junction

We begin by observing the path selection behaviors of liquid front at a cross junction. As shown in Figs. 2(a)–2(c), three distinct flow types are identified, namely, (a) straight, (b) diverging, and (c) diverting flow. The straight flow corresponds to a liquid front continuing in its original propagation direction along the main channel, neglecting branches. The diverging flow is characterized by the liquid front diverging at the junction and propagating through both the main and branch channels. In the diverted flow, the front abruptly stops advancing in the main channel but rather propagates solely into the branches. We observed the flow type transition from straight to diverging flow and finally to diverted flow as the liquid's injection flow rate Q is reduced (d), or as the branch channel width w_b is increased (e), with the other conditions kept the same.

To understand the physical mechanisms behind those path selection modes of the liquid front, we first analyze the forces dominating the interfacial flow. The Reynolds number, a ratio of flow inertia to viscosity, $\mathrm{Re} = \rho U D_m/\mu$ has the order of $10 - 10^2$, with an average injection flow velocity of $U = Q/(hw_m) \sim 10^{-2} - 10^{-1}$ m s^{-1} based on the hydraulic diameter of the main channel $D_m = 2w_m h/(w_m + h) \sim 10^{-3}$ m. The Weber number, a ratio of inertia to surface tension force, $\mathrm{We} = \rho U^2 D_m/\sigma$ has the order of $10^{-2} - 1$. The Ohnesoge number, a ratio of viscous force to the product of inertia and surface tension force, $\mathrm{Oh} = \mu/\sqrt{\rho\sigma D_m}$ has the order of 10^{-3}. This low Ohnesorge number indicates that in our system, inertia and surface tension dominate over viscosity.[35] With the Bond number, a ratio of the gravitational forces to surface tension forces, $\mathrm{Bo} = \rho g D_m^2/\sigma$ being nearly 1, we observed the side view of the meniscus in the yz-plane as shown in Fig. 3(c) to investigate the gravitational effects. We see that the meniscus deflection is insignificant, allowing us to neglect the curvature in the yz-plane. Hence, we find the flow to be primarily governed by inertia rather than viscosity, while interfacial forces significantly affect the behavior of the liquid front.

Figures 3(a)–3(d) depict a meniscus profile formed at the junction of the main and branch channels. While the orientation angle of the meniscus at the contact line ϕ is less than the critical orientation angle ϕ_c, the contact line is pinned with the meniscus bulging as liquid keeps being supplied at the constant flow rate.[36,37] Upon ϕ reaching ϕ_c, the liquid front begins to wet the branching channel wall [marked yellow in Fig. 3(a)], which we refer to as burst. We measured the critical orientation angle of the meniscus, $\phi_{c,v}$, for the vertical plane and $\phi_{c,h}$ for the horizontal plane, by observing the maximum angle

TABLE I. Physical properties of dyed aqueous ethanol solutions at 23 °C (average value of five measurements ± standard deviation).

Liquid	A	B	C	D	E
Ethanol volume concentration (%)	0	5	10	15	25
Density (kg/m^3)	984 ± 73	978 ± 53	966 ± 38	945 ± 45	920 ± 30
Viscosity (mPa s)	1.01 ± 0.05	1.11 ± 0.02	1.28 ± 0.07	1.45 ± 0.10	1.96 ± 0.10
Surface tension (mN/m)	71.3 ± 0.4	56.6 ± 0.2	50.6 ± 0.2	44.9 ± 0.2	36.8 ± 0.5
Static contact angle (deg)	7 ± 2	8 ± 1	8 ± 1	8 ± 1	8 ± 2
Critical advancing contact angle (deg)	24 ± 5	16 ± 4	14 ± 2	12 ± 3	9 ± 1

20 March 2025 13:25:23

Published under an exclusive license by AIP Publishing

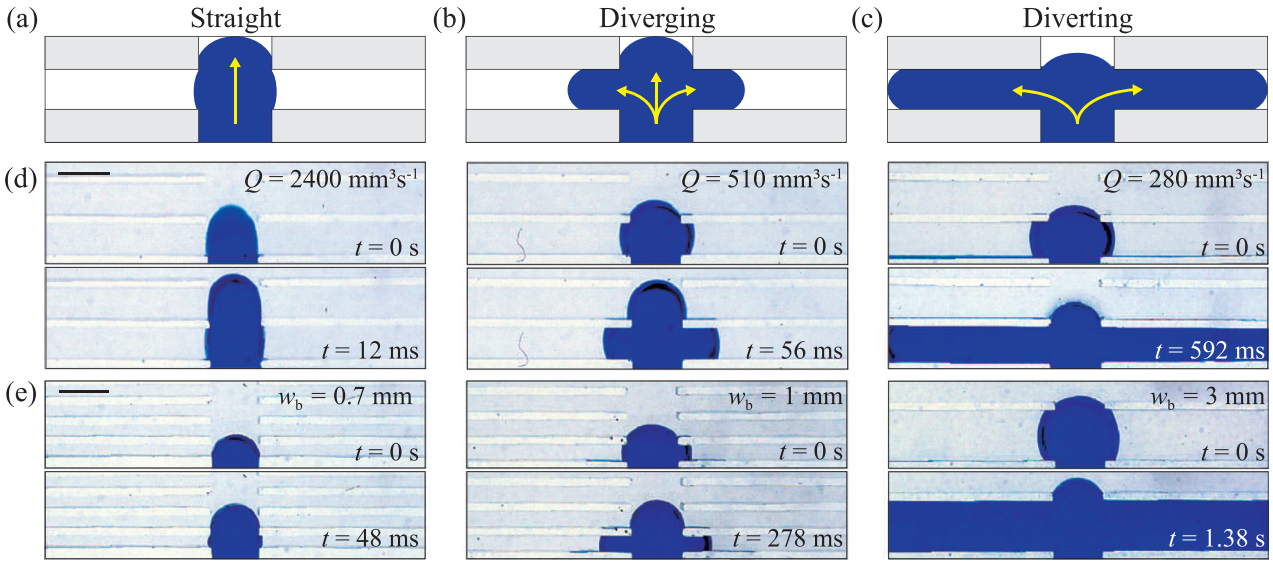

FIG. 2. (a)–(c) Illustration of the three types of liquid front propagation at a branch junction. (a) Straight flow; (b) diverging flow; and (c) diverting flow. The transition of front propagation types from straight to diverging to diverting flow, (d) as the injection flow rate of the liquid decreases ($w_m = 3$, $w_b = 2$ mm), and (e) as the branch channel width increases ($w_m = 3$ mm, $Q = 300\,\mathrm{mm^3\,s^{-1}}$). Liquid A is used in (d) and (e). Scale bars, 3 mm.

between the main channel wall at the junction entrance and the tangential line of liquid–gas interface, as illustrated in Fig. 3(b). These measurements were conducted using various liquids at a constant flow rate. The results are detailed in Table II.

The shape of meniscus is inherently three-dimensional, giving the total curvature $\kappa = \kappa_v + \kappa_h$. Here, $\kappa_v = 2\sigma \cos \phi_{c,v}/w_m$ represents the vertical curvature in the yz-plane, and $\kappa_h = 2\sigma \cos \phi_{c,h}/h$ denotes the horizontal curvature in the xy-plane, as depicted in Fig. 3(b).

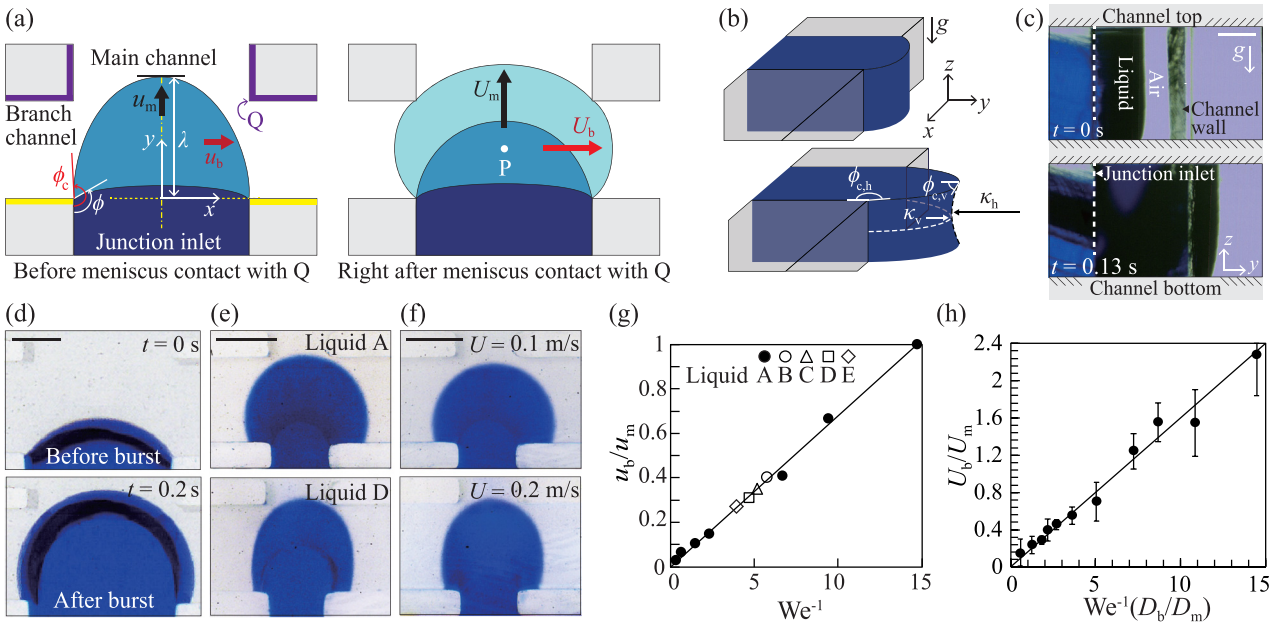

FIG. 3. (a) 2D schematic, (b) 3D schematic, and experimental images of a meniscus profile at a branch junction, showing (c) side view and (d) top view. The liquid front grows faster toward the branch channel (e) when the surface tension is higher and (f) when the average velocity is lower. In (c) and (d), liquid A was used in a channel with dimensions $[w_m, w_b] = [3, 2]$ mm. For (e), liquids A and D were tested in a channel of $[w_m, w_b] = [1, 1.5]$ mm, while (f) used liquid A in the same channel dimensions. Scale bars, 1 mm. (g) The experimental data for the ratio of the velocity toward the branch to the velocity toward the main channel (before meeting the next corner), u_b/u_m, vs We^{-1} in a channel with $[w_m, w_b] = [1, 1.5]$ mm. (h) The experimental data for the velocity ratio U_b/U_m vs the combined parameter, $\mathrm{We}^{-1}(D_b/D_m)$.

20 March 2025 13:25:23

Published under an exclusive license by AIP Publishing

TABLE II. Critical orientation angle of the meniscus, $\phi_{c,h}$ and $\phi_{c,v}$, for the horizontal (*xy*) and vertical (*yz*) planes, respectively. These angles were measured by injecting liquids into a channel with dimensions $[w_m, w_b] = [3, 2]$ mm at a constant flow rate of 840 mm^3/s (average value of five measurements ± standard deviation).

Liquid	A	B	C	D	E
Ethanol volume concentration (%)	0	5	10	15	25
Horizontal critical orientation angle, $\phi_{c,h}$ (deg)	196 ± 2	191 ± 3	187 ± 4	184 ± 4	181 ± 4
Vertical critical orientation angle, $\phi_{c,v}$ (deg)	99 ± 7	87 ± 5	84 ± 5	81 ± 2	78 ± 4

Table II shows that the value of $\cos\phi_{c,h}$ is significantly larger than $\cos\phi_{c,v}$, indicating the importance of the horizontal meniscus curvature, κ_h, in analyzing the liquid front behavior at junctions. Additionally, we experimentally found that this horizontal meniscus shape was kept elliptic even after burst, as shown in Fig. 3(d). Assuming the shape of the meniscus from top view as a semi-ellipse centered at the middle of the junction inlet, the curvature κ from top view is scaled as $\kappa \sim \lambda/w_m^2$, where λ is the *y*-directional distance from the center to the meniscus vertex. Because the interfacial tension is resisting the inertial force, we balance the capillary pressure $p_c \sim \sigma\kappa$ with the dynamic pressure $p_d \sim \rho U^2$, which gives $\lambda/w_m \sim \mathrm{We}$. The continuity equation for the liquid flow then allows us to write $u_m/\lambda \sim u_b/w_m$, where u_m and u_b are the flow velocities toward the main channel and the branches, respectively. Thus, we can get a scaling relation for the ratio of the *x*-directional liquid velocity (to the branching channel), u_b, to the main flow velocity, u_m, as

$$\frac{u_b}{u_m} \sim \frac{1}{\mathrm{We}}. \tag{1}$$

Figure 3(e) reveals that the liquid front tends to grow faster toward the branching channel (horizontally) than toward the main channel (vertically) for higher surface tension (σ of liquid A is higher than of liquid D). The faster growth toward the branch channel is also observed for lower injection flow velocity [Fig. 3(f)]. These observations are consistent with relation (1). We measured u_m and u_b by tracking the displacement of the liquid front from the y axis for u_b and the x axis for u_m just before the front reached the next corners (Q) colored violet in Fig. 3(a). We plot their ratio, u_b/u_m, as a function of We^{-1} in Fig. 3(g), which shows good agreement between our theory and experiment.

Once the bulging meniscus meets the new corner, the ratio of the velocities to the branch and main channels was found to be modified as a function of the widths of main and branch channels. It is because the hydrophilic channel walls tend to draw the meniscus to their sides, with the capillary force from the branch and main channels being scaled as σD_b and σD_m, respectively. Here, $D_b = 2w_b h/(w_b + h)$ is the hydraulic diameter of the branch channel. Thus, we speculate that the ratio of the capillary forces D_b/D_m affects the velocity ratio U_b/U_m. Here, U_b and U_m, respectively, correspond to the average velocity of meniscus front toward the branch and main channels, measured from when the meniscus reaches the center of the junction (P) until it attempts further penetration into the channel after touching the next channel walls (Q) in Fig. 3(a). Based on relation (1) and the consideration of capillary force ratio, we experimentally tested the velocity ratio written as

$$\frac{U_b}{U_m} \sim \frac{1}{\mathrm{We}}\frac{D_b}{D_m}. \tag{2}$$

Figure 3(h) shows that the velocity ratio, indeed, follows relation (2) validating our assumption.

B. Regime map of liquid front behaviors

As liquid fronts traverse the junction, they continually meet the inlet of new main and branch channels. Here, the contact line can be either pinned or advanced, determined by the competition of capillary pressure and dynamic pressure in each direction, as illustrated in Fig. 4(a). The capillary pressure peaks at the critical orientation angle of the meniscus, given by $p_c \sim \sigma\cos\phi_c/D$. For the liquid front to penetrate any channel, the dynamic pressure must exceed the capillary pressure. If the dynamic pressure is insufficient, the progression of the liquid front into the corresponding channel is restrained. Thus, the dynamic-to-capillary pressure ratio governs the directionality of the liquid front after meeting the junction.

We consider the dynamic-to-capillary pressure ratio at the inlet of the branch channel, $p_{d,b}/p_{c,b} \sim \rho U_b^2 D_b/(\sigma\cos\phi_c)$. At the branch channel's inlet, the critical orientation angle of the meniscus with the four channel walls ϕ_c becomes equal to the vertical critical orientation angle of the meniscus $\phi_{c,v}$. If $p_{d,b}/p_{c,b} < 1$, the liquid front is prevented from advancing to the branch channel, resulting in a straight flow, as shown in Fig. 4(b). Given $U_m \sim U$ and the scaling relation (2), the velocity of the liquid front at the junction propagating to the branch channel $U_b \sim \sigma D_b/(\rho U D_m^2)$. Substituting U_b into $p_{d,b} < p_{c,b}$ yields the condition for the straight flow:

$$\frac{D_b}{D_m} < k_s \mathrm{We}^{1/3}\cos^{1/3}\phi_{c,v}, \tag{3}$$

where k_s is a prefactor to be determined empirically.

Similarly, for the dynamic-to-capillary pressure ratio at the main channel inlet, the liquid front cannot advance further to the main channel if $p_{d,m}/p_{c,m} \sim \rho U_m^2 D_m/(\sigma\cos\phi_c) < 1$. At the main channel inlet, primarily due to the almost negligible channel length and the consequent proximity to the subsequent junction, the critical orientation angle of the meniscus, ϕ_c, corresponds to the horizontal critical orientation angle $\phi_{c,h}$. Consequently, the incoming liquid primarily flows into the branch channels, and we write the velocity $U_b \sim UD_m/D_b$ via continuity. This corresponds to the diverting flow, as shown in Fig. 4(c). The velocity of the liquid front propagating to the main channel from the junction, U_m, is scaled as $\rho U^3 D_m^3/(\sigma D_b^2)$ using the continuity and relation (2). Then, the pressure ratio condition allows us to predict the diverting flow when

$$\frac{D_b}{D_m} > k_d \frac{\mathrm{We}^{3/4}}{\cos^{1/4}\phi_{c,h}} \tag{4}$$

with k_d being a prefactor to be determined empirically.

20 March 2025 13:25:23

Published under an exclusive license by AIP Publishing

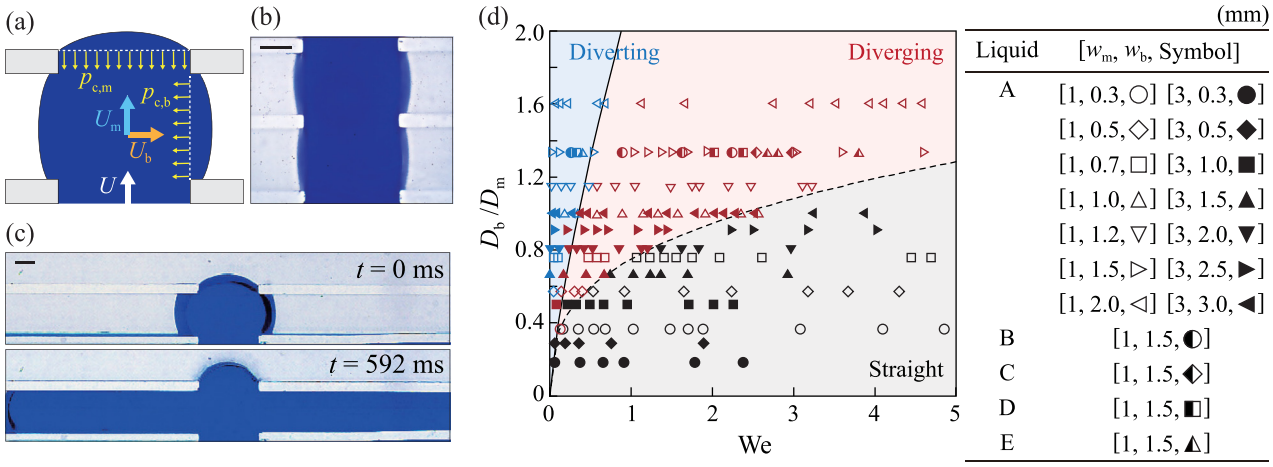

FIG. 4. (a) Schematics of the liquid front after meeting the next junction wall, with its directionality governed by the relative magnitude of capillary and dynamic pressure. (b) Straight flow where the liquid front continuously propagates straight through the main channel. (c) Diverting flow where the liquid front cannot advance toward the main channel but propagates exclusively through the branch channels. Scale bars, 1 mm. Experiments in (b) and (c) were conducted using liquid A. For (b), a flow rate of $Q = 1000\,\mathrm{mm}^3\,\mathrm{s}^{-1}$ and channel dimensions of $[w_m, w_b] = [3, 2]$ mm were used. For (c), the flow rate was $Q = 180\,\mathrm{mm}^3\,\mathrm{s}^{-1}$ with channel dimensions of $[w_m, w_b] = [3, 3]$ mm. (d) Regime map of the flow in branching channels, constructed by the Weber number, We, and the hydraulic diameter ratio between the branch and main channels D_b/D_m. The solid line from relation (4) marks the boundary between the diverting and diverging flow, and the dotted line from relation (3) corresponds to the boundary between the diverging and straight flow. The colors of symbols correspond to the different flow regimes: straight flow (black), diverging flow (red), and diverting flow (blue).

Our theoretical analysis suggests two primary factors that guide the direction of liquid front propagation in branching channels of given surface condition (fixed ϕ): the Weber number and the channel geometry. The channel geometry that satisfies neither of inequalities (3) or (4) allows the liquid front to propagate into both the main and branching channels, giving rise to the diverging flow. We experimentally observed the propagation direction of liquid fronts under a variety of conditions, including different liquid properties, injection flow rates, and the hydraulic diameter ratio of the branch to the main channel. The experimental results are captured in a regime map, created in a two-dimensional space defined by the Weber number and the hydraulic diameter ratio, as shown in Fig. 4(d). The map demarcates the regimes for straight (black symbols), diverging (red symbols), and diverting (blue symbols) flows. The theoretically predicted boundaries, marking transitions from straight to diverging and from diverging to diverting flows, were obtained from inequalities (3) and (4) with the prefactors being $k_s = 1.4$ and $k_d = 2$. These boundaries neatly divide the flow regimes, verifying our theoretical model.

Our regime map shows that the diverting flow occurs only in a low We region, while the liquid front tends to flow straight to the main channel neglecting branches when We is high and D_b/D_m is small. The diverging flow tends to arise when the branching channels are wide compared to the main channel, with its range located between the straight and diverting regime.

C. Flow patterns in multi-branching channels

The consequence of different path selection behaviors at branch junctions is a variety of liquid-filling patterns in multi-branching channels. These patterns primarily depend on the propagation direction chosen at the first junction of the multi-branching channel. When the straight flow occurs at this junction, the liquid injected at a constant flow rate maintains its initial velocity at all subsequent junctions without losing any volume to the branch channels. Thus, we see only a main channel filled with liquid leaving the branch channels unfilled, as shown in Fig. 5(a).

This straight filling pattern bears practical significance when the liquid flowing parallel to permeable walls should be deterred from penetrating the walls. Membrane distillation[2,3] provides a good example, where heated sea water provides water vapor to the other side of the separating porous membrane. The prevention of leaking the sea water while allowing passage of vapor through the porous membrane is an important process requirement.

When the liquid front exhibits a diverting flow at the first junction, the liquid exclusively flows into the branches, leaving the main channel empty due to insufficient pressure buildup. As the branch channels are finite in length, the liquid in those channels eventually meets an open atmosphere at the end of the channel, where the liquid should choose whether to burst the capillary-force barrier at the branch channel end or to invade the main channel. Our channel design is such that the liquid prefers invading the hydrophilic main channel rather than wetting the outside wall at the branch channel end. The diverting occurs whenever the main channel meets a branch junction because of the constant flow rate injection. Thus, the liquid-filling pattern in this regime is as shown in Fig. 5(c).

Such a filling pattern is beneficial when the liquid needs to reach different destinations at designated times, with specific time intervals. This filling pattern could be utilized in a multi-step chemical reaction process,[22] where reactants need to be sequentially introduced to each branch at different times. Since the liquid flows only through the channels connected to a single junction until it reaches the end of those channels, we can control the timing of liquid delivery at different locations by manipulating the junction number and channel length.

Under the diverging flow condition, the liquid front propagates through the main channel while simultaneously filling the branches, as shown in Fig. 5(b). The pattern arising in the course of liquid filling is

20 March 2025 13:25:23

Published under an exclusive license by AIP Publishing

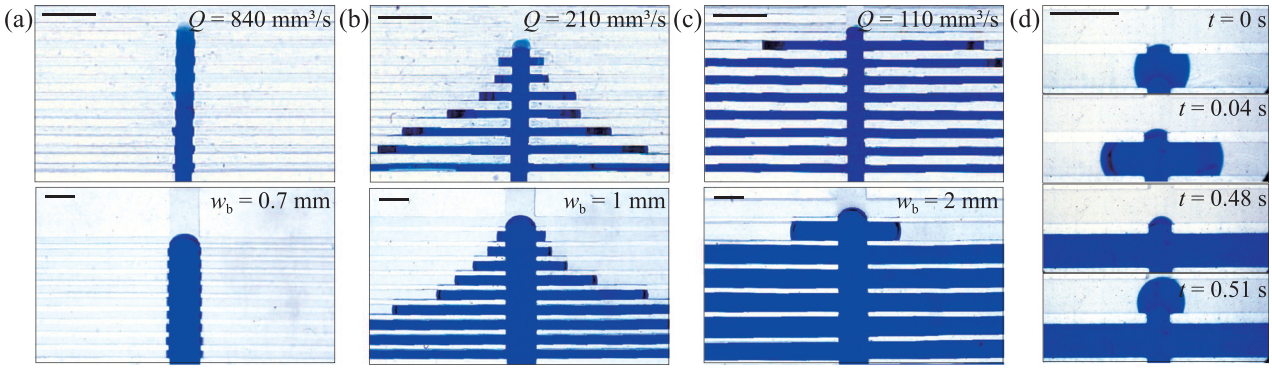

FIG. 5. (a) Straight flow in multi-branching channels, leaving the branches unfilled. (b) Diverging flow, where the liquid front propagates through the main channel while simultaneously filling the branches. (c) Stepwise filling pattern in multi-branching channels owing to the diverting flow behavior. (d) Temporal evolution of the liquid front during diverting flow; the liquid front propagates only through the branch channels until reaching the branches' terminal open ends ($t = 0.48$ s) and then advances to the next junction. The experiments in (a)–(d) were performed with liquid A. Those in the top row of (a)–(c), a channel with dimensions $[w_m, w_b] = [1, 0.5]$ mm was used, while those on the bottom row, it was used $Q = 300\,\mathrm{mm}^3\,\mathrm{s}^{-1}$ in a channel with $[w_m, w_b] = [3, 0.5]$ mm. Experiment (d) employed $Q = 180\,\mathrm{mm}^3\,\mathrm{s}^{-1}$ in a $[w_m, w_b] = [1, 1.5]$ mm channel. Scale bars, 3 mm.

reminiscent of a Christmas tree, where the filled length of horizontal branches gets shorter downstream. If the constant flow rate injection is maintained, all the branches will be completely filled eventually.

This filling pattern is useful when we need partitioning and distribution of liquid across all connected locations. This is notably relevant in such microfluidic devices as digital nucleic acid assay chips, where a number of microwells should be automatically loaded with liquid from a liquid source.[28,29] Microwells connected at the ends of the branching channels can be loaded with the liquid supplied under the diverging flow condition.

IV. CONCLUSION

We have investigated the path selection dynamics of a liquid front propagating in branching channels. As the flows of our interest are dominated by inertia and surface tension, the front behavior has been shown to depend on the Weber number and the channel geometry represented by the hydraulic diameter ratio of the main and branch channels. The three distinct flow regimes have been identified, namely, straight, diverging, and diverting flows, and the theoretical models to find the regime boundaries have been constructed. The regime map states that the straight flow tends to arise when the flow inertia along the main channel dominates over the capillary-force induced obstruction to pass the channel junctions. The diverting flow occurs when the liquid is forced to divert to the branch channel as the flow toward the main channel is frustrated by the capillary obstruction. The diverging flow regime is located between the straight and diverting regimes.

The resulting liquid-filling patterns of the channel network allows us to obtain various modes of liquid delivery at the channel ends as well as different shapes of liquid sculpture. Because our theoretical and experimental results enable us to control liquid distribution and delivery in channel networks, a range of practical applications can emerge using our technology, including design of porous membranes for liquid separation and microfluidic chips with multiple sites for chemical reaction.

Although we have supplied liquid into the channel network with a syringe pump to achieve the constant flow rate, thus the constant Weber number, we can consider the case where the constant pressure source is employed. Then, the velocity of the liquid front will keep decreasing as it propagates due to viscous dissipation, suggesting a possibility that the straight flow in the beginning gradually transitions to diverging and then diverting flow. We can also think about different ways to obtain various liquid filling patterns by modulating the injection flow rate or pressure magnitude *in situ*, spatially patterning the wettability or dimensions of channel walls, which will further enrich the applications of liquid front steering technology in milli- and microfluidic systems.

ACKNOWLEDGMENTS

This work was supported by the Basic Science Research Program through the National Research Foundation funded by the Ministry of Education (Grant No. 2022-R1I1A1A01066046) and the Ministry of Science and ICT (Grant Nos. 2018-052541 and 2021-017476), Korea.

AUTHOR DECLARATIONS

Conflict of Interest

The authors have no conflicts to disclose.

Author Contributions

Sohyun Jung and Tae Jeong Kim contributed equally to this work.

Sohyun Jung: Formal analysis (lead); Writing – original draft (lead). **Tae Jeong Kim:** Investigation (lead); Methodology (lead). **Jae Hong Lee:** Investigation (supporting); Methodology (supporting); Validation (supporting). **Wonjong Jung:** Conceptualization (lead); Validation (lead). **Ho-Young Kim:** Formal analysis (supporting); Supervision (lead); Writing – review & editing (lead).

DATA AVAILABILITY

The data that support the findings of this study are available from the corresponding author upon reasonable request.

20 March 2025 13:25:23

Published under an exclusive license by AIP Publishing

REFERENCES

[1]D. J. Beebe, G. A. Mensing, and G. M. Walker, "Physics and applications of microfluidics in biology," Annu. Rev. Biomed. Eng. **4**, 261–286 (2002).
[2]K. W. Lawson and D. R. Lloyd, "Membrane distillation," J. Membr. Sci. **124**, 1–25 (1997).
[3]L. Eykens, K. De Sitter, C. Dotremont, L. Pinoy, and B. Van der Bruggen, "How to optimize the membrane properties for membrane distillation: A review," Ind. Eng. Chem. Res. **55**, 9333–9343 (2016).
[4]M. K. Um and W. I. Lee, "A study on the mold filling process in resin transfer molding," Polym. Eng. Sci. **31**, 765–771 (1991).
[5]D. J. Coyle, J. W. Blake, and C. W. Macosko, "The kinematics of fountain flow in mold–filling," AIChE J. **33**, 1168–1177 (1987).
[6]E. Detournay, "Mechanics of hydraulic fractures," Annu. Rev. Fluid Mech. **48**, 311–339 (2016).
[7]D. A. Mendelsohn, "A review of hydraulic fracture modeling—Part I: General concepts, 2D models, motivation for 3D modeling," J. Energy Resour. Technol. **106**, 369–376 (1984).
[8]E. W. Washburn, "The dynamics of capillary flow," Phys. Rev. **17**, 273–283 (1921).
[9]J. Ha and H.-Y. Kim, "Capillarity in soft porous solids," Annu. Rev. Fluid Mech. **52**, 263–284 (2020).
[10]J. Kim and H. Y. Kim, "On the dynamics of capillary imbibition," J. Mech. Sci. Technol. **26**, 3795–3801 (2012).
[11]J. H. Snoeijer and B. Andreotti, "Moving contact lines: Scales, regimes, and dynamical transitions," Annu. Rev. Fluid Mech. **45**, 269–292 (2013).
[12]R. L. Hoffman, "A study of the advancing interface. I. Interface shape in liquid–gas systems," J. Colloid Interface Sci. **50**, 228–241 (1975).
[13]C. Huh and L. E. Scriven, "Hydrodynamic model of steady movement of a solid/liquid/fluid contact line," J. Colloid Interface Sci. **35**, 85–101 (1971).
[14]R. J. Hansen and T. Y. Toong, "Dynamic contact angle and its relationship to forces of hydrodynamic origin," J. Colloid Interface Sci. **37**, 196–207 (1971).
[15]R. L. Cerro, "Moving contact lines and Langmuir–Blodgett film deposition," J. Colloid Interface Sci. **257**, 276–283 (2003).
[16]E. Mitsoulis, "Fountain flow revisited: The effect of various fluid mechanics parameters," AIChE J. **56**, 1147–1162 (2010).
[17]B. Zhao, A. A. Pahlavan, L. Cueto-Felgueroso, and R. Juanes, "Forced wetting transition and bubble pinch-off in a capillary tube," Phys. Rev. Lett. **120**, 084501 (2018).
[18]C. Colosi, S. R. Shin, V. Manoharan, S. Massa, M. Costantini, A. Barbetta, M. R. Dokmeci, M. Dentini, and A. Khademhosseini, "Microfluidic bioprinting of heterogeneous 3D tissue constructs using low-viscosity bioink," Adv. Mater. **28**, 677–684 (2016).
[19]N. A. Dudukovic, E. J. Fong, H. B. Gemeda, J. R. DeOtte, M. R. Cerón, B. D. Moran, J. T. Davis, S. E. Baker, and E. B. Duoss, "Cellular fluidics," Nature **595**, 58–65 (2021).
[20]J. Ko, Y. Lee, S. Lee, S. R. Lee, and N. L. Jeon, "Human ocular angiogenesis–inspired vascular models on an injection–molded microfluidic chip," Adv. Healthcare Mater. **8**, 1900328 (2019).
[21]B. Lee, S. Kim, J. Ko, S.-R. Lee, Y. Kim, S. Park, J. Kim, S. Hyung, H.-Y. Kim, and N. L. Jeon, "3D micromesh-based hybrid bioprinting: Multidimensional liquid patterning for 3D microtissue engineering," NPG Asia Mater. **14**, 6 (2022).
[22]M. Yafia, O. Ymbern, A. O. Olanrewaju, A. Parandakh, A. Sohrabi Kashani, J. Renault, Z. Jin, G. Kim, A. Ng, and D. Juncker, "Microfluidic chain reaction of structurally programmed capillary flow events," Nature **605**, 464–469 (2022).
[23]S. Li, Z. Ma, Z. Cao, L. Pan, and Y. Shi, "Advanced wearable microfluidic sensors for healthcare monitoring," Small **16**, 1903822 (2020).
[24]R. K. Arun, S. Halder, N. Chanda, and S. Chakraborty, "A paper based self-pumping and self-breathing fuel cell using pencil stroked graphite electrodes," Lab Chip **14**, 1661–1664 (2014).
[25]S. S. Das, S. Kar, T. Anwar, P. Saha, and S. Chakraborty, "Hydroelectric power plant on a paper strip," Lab Chip **18**, 1560–1568 (2018).
[26]A. Olanrewaju, M. Beaugrand, M. Yafia, and D. Juncker, "Capillary microfluidics in microchannels: From microfluidic networks to capillaric circuits," Lab Chip **18**, 2323–2347 (2018).
[27]J. Hu, L. Chen, P. Zhang, K. Hsieh, H. Li, S. Yang, and T. H. Wang, "A vacuum-assisted, highly parallelized microfluidic array for performing multi-step digital assays," Lab Chip **21**, 4716–4724 (2021).
[28]H. Tachibana, M. Saito, K. Tsuji, K. Yamanaka, and E. Tamiya, "Self-propelled continuous-flow PCR in capillary-driven microfluidic device: Microfluidic behavior and DNA amplification," Sens. Actuators B **206**, 303–310 (2015).
[29]X. Gao, J. Li, C. Li, Z. Zhang, W. Zhang, J. Yao, M. Guan, Z. Guo, C. Li, and L. Zhou, "High filling rate digital PCR through-hole array chip with double independent S-shaped flow channels," Biomicrofluidics **14**, 034109 (2020).
[30]S. Han and K. K. Wang, "Analysis of the flow of encapsulant during underfill encapsulation of flip-chips," IEEE Trans. Compon. Packag. Manuf. Technol. Part B **20**, 424–433 (1997).
[31]C. Y. Khor, M. A. Mujeebu, M. Z. Abdullah, and F. C. Ani, "Finite volume based CFD simulation of pressurized flip-chip underfill encapsulation process," Microelectron. Reliab. **50**, 98–105 (2010).
[32]J. Tóth, *Gravitational Systems of Groundwater Flow: Theory, Evaluation, Utilization* (Cambridge University Press, Cambridge, 2009).
[33]J. M. Hunt, "Generation and migration of petroleum from abnormally pressured fluid compartments," AAPG Bull. **74**, 1–12 (1990).
[34]J. F. Oliver, C. Huh, and S. G. Mason, "Resistance to spreading of liquids by sharp edges," J. Colloid Interface Sci. **59**, 568–581 (1977).
[35]M. Do-Quang, J. Shiomi, and G. Amberg, "When and how surface structure determines the dynamics of partial wetting," Europhys. Lett. **110**, 46002 (2015).
[36]H. Cho, H.-Y. Kim, J. Y. Kang, and T. S. Kim, "How the capillary burst microvalve works," J. Colloid Interface Sci. **306**, 379–385 (2007).
[37]W. J. A. de Wijs, J. Laven, and G. de With, "Wetting forces and meniscus pinning at geometrical edges," AIChE J. **62**, 4453–4465 (2016).

20 March 2025 13:25:23

Published under an exclusive license by AIP Publishing